LETTER

doi:10.1038/nature13694

Hierarchical organization of chiral rafts in colloidal membranes

Prerna Sharma[1]*, Andrew Ward[1]*, T. Gibaud[2], Michael F. Hagan[1] & Zvonimir Dogic[1]

Liquid–liquid phase separation is ubiquitous in suspensions of nanoparticles, proteins and colloids. It has an important role in gel formation, protein crystallization and perhaps even as an organizing principle in cellular biology[1,2]. With a few notable exceptions[3,4], liquid–liquid phase separation in bulk proceeds through the continuous coalescence of droplets until the system undergoes complete phase separation. But when colloids, nanoparticles or proteins are confined to interfaces, surfaces or membranes, their interactions differ fundamentally from those mediated by isotropic solvents[5,6], and this results in significantly more complex phase behaviour[7–13]. Here we show that liquid–liquid phase separation in monolayer membranes composed of two dissimilar chiral colloidal rods gives rise to thermodynamically stable rafts that constantly exchange monomeric rods with the background reservoir to maintain a self-limited size. We visualize and manipulate rafts to quantify their assembly kinetics and to show that membrane distortions arising from the rods' chirality lead to long-range repulsive raft–raft interactions. Rafts assemble into cluster crystals at high densities, but they can also form bonds to yield higher-order structures. Taken together, our observations demonstrate a robust membrane-based pathway for the assembly of monodisperse membrane clusters that is complementary to existing methods for colloid assembly in bulk suspensions[14–16]. They also reveal that chiral inclusions in membranes can acquire long-range repulsive interactions, which might more generally have a role in stabilizing assemblages of finite size[13,17].

In the presence of a non-adsorbing polymer, monodisperse rod-like viruses experience effective depletion attractions that drive their lateral association. These interactions can lead to the assembly of colloidal monolayer membranes, one rod-length thick, that are held together by the osmotic pressure of the enveloping polymer suspension[18]. Colloidal monolayers and lipid bilayers exhibit long-wavelength fluctuations described by the same free energy, despite their molecular-scale differences.

In this work we investigated the behaviour of colloidal membranes containing a mixture of two rods: rod-like *fd*-Y21M virus (880 nm long) and M13KO7 virus (1,200 nm long)[19]. Membranes were assembled by adding a depletant to a dilute isotropic mixture of *fd*-Y21M and M13KO7. After reaching a large enough size, membranes sedimented to the bottom of the sample chambers; the constituent rods pointed in the *z* direction and images were taken in the *x*–*y* plane (Fig. 1). For all parameters investigated, both rods co-assembled into the same colloidal membrane. At low depletant concentration the rods remained homogeneously mixed throughout the membrane (Fig. 1b, d), whereas at high depletant concentration they separated into bulk phases (Fig. 1b, f). At intermediate concentrations we observed the formation of highly monodisperse micrometre-sized droplets (colloidal rafts) enriched in short rods and floating in the background of long rods (Fig. 1e). Colloidal rafts did not coarsen with time, suggesting that they were equilibrium structures.

To test this hypothesis we brought two membranes, each containing only one type of virus, into close proximity (Fig. 1a). On coalescence, the interface separating dissimilar rods became unstable as short rods invaginated into the long-rod fluid, giving rise to an interconnected network of rafts held together by thin metastable bridges (Fig. 1c and Supplementary Video 1). Over time the conjoining liquid bridges disintegrated, leading to the formation of isolated finite-sized rafts and demonstrating

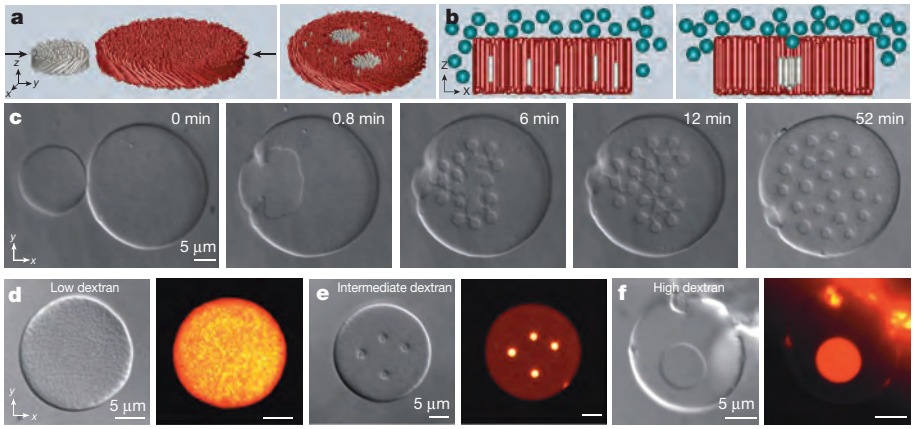

Figure 1 | Membrane-mediated assembly of monodisperse chiral colloidal rafts. a, Coalescence of membranes composed of short and long rods of opposite chiralities. **b**, Clustering of short rods dissolved in a long-rod membrane is driven by excluded-volume interactions. **c**, Coalescence of short right-handed *fd*-Y21M and long left-handed M13KO7 membranes leads to the formation of finite-sized rafts. **d**, Differential interference contrast and fluorescence images of a *fd*-Y21M–MK13KO7 membrane at 34 mg ml^{-1} dextran concentration show homogeneous mixing. *fd*-Y21M is fluorescently labelled. **e**, Formation of finite-sized clusters enriched in fluorescently labelled *fd*-Y21M at intermediate dextran concentrations (38 mg ml^{-1}). The background hue indicates that a small fraction of *fd*-Y21M rods are dissolved in the background membrane. **f**, Complete separation of the bulk phase is observed at the highest dextran concentrations (52 mg ml^{-1}).

[1]Department of Physics, Brandeis University, 415 South Street, Waltham, Massachusetts 02454, USA. [2]Laboratoire de Physique, École Normale Supérieure de Lyon, Université de Lyon I, CNRS/UMR 5672, 46 allée d'Italie, 69007 Lyon, France.
*These authors contributed equally to this work.

that colloidal rafts have a lower free energy than a bulk separated phase. We have explored the behaviour of six phase-separating mixtures composed of viruses of various physical properties; in each case we observed micro-separated phases at intermediate polymer concentrations, suggesting that rafts are a ubiquitous feature of colloidal membranes (Methods). Here we focus on the behaviour of the *fd*-Y21M–M13KO7 mixture, using the unique features of colloidal membranes that allow us to manipulate rafts optically, to visualize their nucleation pathways and to track the real-space dynamics of isolated constituent rods.

We determined the raft free-energy landscape by measuring how k_{on} and k_{off}, the rates at which rods associate and dissociate from a raft, depend on the raft size. We measured k_{off} using fluorescence recovery after photobleaching (FRAP)[20]. Using a focused beam, we bleached an isolated raft of predetermined size. The fluorescence signal recovered within minutes, indicating an exchange of bleached raft-bound rods with unbleached background rods (Fig. 2a and Supplementary Video 2). The fluorescence recovery curves were fitted by single-exponential curves (Fig. 2e). If the raft size does not change appreciably during of experiment, the fluorescence recovery time constant is $1/k_{off}$ (Methods). By performing FRAP measurements on rafts of varying radii we determined the dependence of k_{off} on raft size (Fig. 2h).

To measure k_{on} we created a raft population with heterogeneous radii R and quantified their subsequent growth rates (Fig. 2b, c, f and Supplementary Video 3). Rafts with $R < R_{critical}$ quickly evaporated into the background membrane (Fig. 2g). When $R_{equilibrium} > R > R_{critical}$, rafts grew until attaining the equilibrium size. Finally, rafts with $R > R_{equilibrium}$ shrank slowly until achieving equilibrium. The evolution of raft size is governed by the kinetic equation

$$\frac{dN(t)}{dt} = -k_{off}N(t) + k_{on}C_{BG}$$

where $N(t)$ is the number of raft-bound rods and C_{BG} is the concentration of short fluorescently labelled rods in the background. $dN(t)/dt$ is determined from size evolution experiments (Fig. 2g), k_{off} is determined through FRAP experiments, and C_{BG} is proportional to the mean fluorescence of the background membrane. The only unknown is k_{on}, making it possible to determine its dependence on raft size. We found that k_{on} increased weakly with increasing raft size, consistent with two-dimensional diffusion-limited association kinetics. Having measured both k_{on} and k_{off} (Fig. 2h), we calculate $\Delta G(N) = k_BT(k_{off}NA_{rod}/k_{on})$, where NA_{rod} is the raft area and $\Delta G(N)$ is the energy cost of adding a single particle to a raft (Fig. 2i). The minimum of the excess free energy satisfies $\Delta G - k_BT\ln(C_{BG}A_{rod}) = 0$ and determines the equilibrium raft size, which corresponds to ~24,000 rods. Integrating ΔG over N reveals how the raft free energy, $G(N)$, scales with the number of rods. The width of the parabola determines the fluctuations in raft area, namely ~1,400 particles, corresponding to fluctuations of 30 nm in radius. Such fluctuations are below the resolution limit of the optical microscope, consistent with our observation of a monodisperse raft distribution in equilibrium.

To validate our analysis independently, we performed single-molecule lifetime experiments by tracking a small fraction of fluorescently labelled

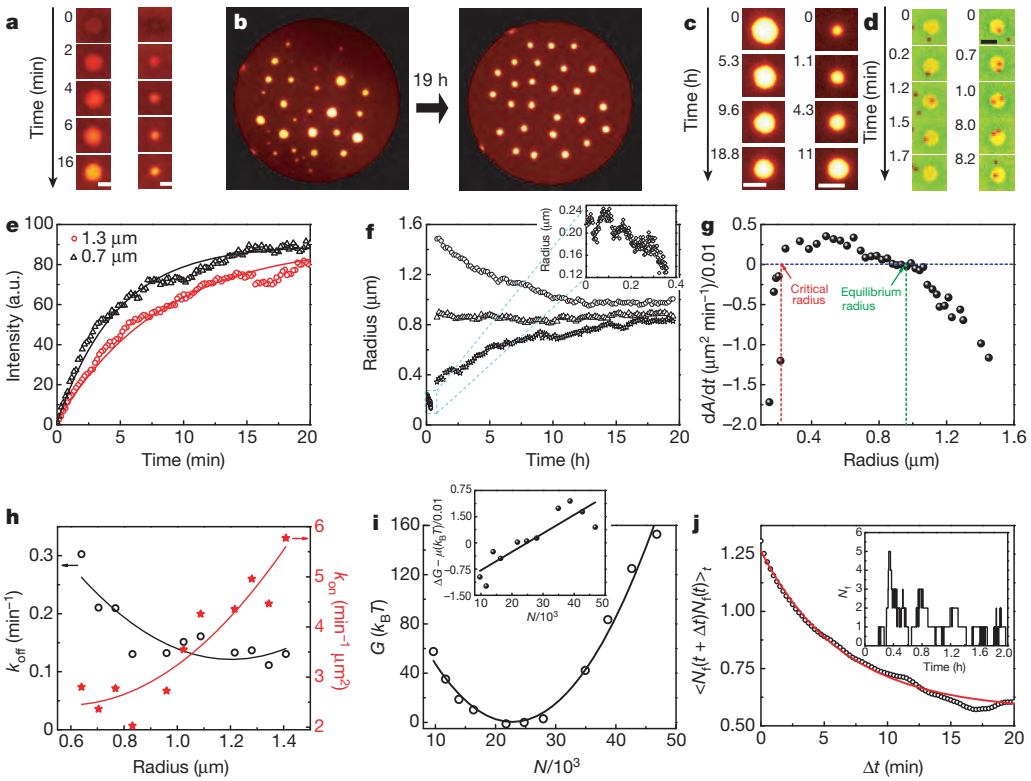

Figure 2 | Single-molecule analysis reveals raft nucleation dynamics and assembly kinetics. **a**, The fluorescence of a bleached cluster recovers after a few minutes, revealing kinetics of rod exchange between rafts and the membrane background. **b**, Initially polydisperse rafts equilibrate in size after many hours. **c**, Expansion of an undersized raft and contraction of an oversized raft. **d**, Fluorescently labelled *fd*-Y21M rods associate and dissociate from a raft, revealing binding kinetics at the single-molecule level. **e**, Exponential recovery of cluster fluorescence intensity after a photobleaching event yields k_{off} for rafts with different sizes. **f**, Time evolution of cluster growth depends on the initial cluster size. Inset: a subcritical raft quickly evaporates into the membrane background. **g**, The dependence of raft expansion rates on raft size directly reveals the critical nucleus size and equilibrium size. **h**, Combining single-raft fluorescence recovery measurements with raft expansion rates reveals the dependence of k_{off} (circles) and k_{on} (stars) on raft size (each point represents a single measurement). **i**, The minimum in raft free-energy landscape indicates the equilibrium raft size. Inset: ΔG, the free-energy change associated with adding a single virus to a colloidal raft (each point represents a single measurement). **j**, Exponential decay of the autocorrelation function of the number of raft-bound rods, $N_f(t)$, yields both k_{off} and k_{on}. For equilibrium-sized rafts, single-molecule analysis agrees with measurements in **h**. Inset: plot of $N_f(t)$. Scale bars, 2.5 μm.

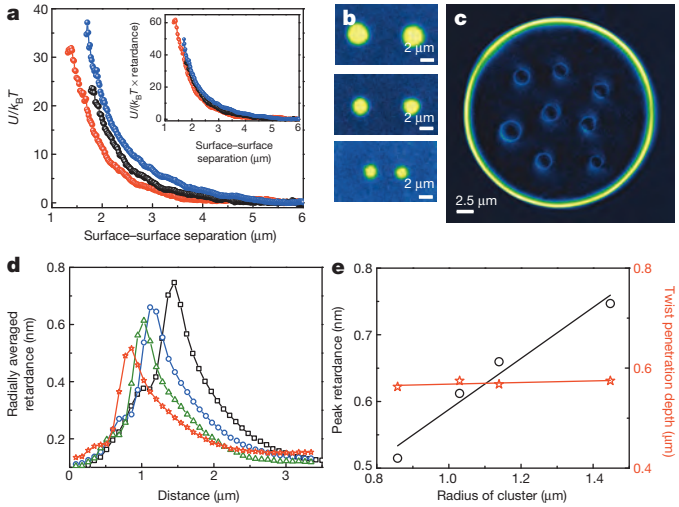

Figure 3 | Raft-induced chiral twist governs membrane-mediated raft repulsions. **a**, Effective pair interaction potential obtained using the blinking trap technique for clusters with diameters of 2.9 μm (blue), 2.1 μm (black) and 1.6 μm (red). Inset: interaction potential rescaled by the maximum tilt angle. **b**, Images of cluster pairs for which interactions were measured. **c**, LC-PolScope image of heterogeneous rafts embedded in a membrane. **d**, Dependence of radially averaged retardance profile on raft size. **e**, Peak retardance (maximum tilt angle; circles) increases linearly with increasing raft size. The twist penetration depth (stars) is independent of domain size (each point represents a single measurement).

short rods in an otherwise unlabelled membrane (Fig. 2d and Supplementary Video 4). Overlaying of fluorescent images onto simultaneously acquired phase-contrast images revealed raft-bound rods as a function of time, $N_f(t)$ (Fig. 2j). From such results we find that for equilibrium rafts $k_{on} = 3.7\ min^{-1}\ \mu m^2$ and $k_{off} = 0.15\ min^{-1}$, which is in agreement with FRAP measurements (Methods). Very few other experimental systems[14,21] permit the visualization of subcritical nucleation dynamics and the measurement of the associated free-energy landscape enabled by our colloidal membranes.

With an understanding of single-raft assembly kinetics, we subsequently measured membrane-mediated raft–raft interactions by adapting a technique based on blinking optical tweezers[22]. To manipulate rafts, which are repelled from a focused laser, we created an optical plough composed of multiple beams. Using two ploughs we pushed a raft pair into close proximity. Subsequently, we switched off the traps and quantified raft trajectories as they were pushed apart by repulsive interactions (Supplementary Video 5). Repeating this procedure dozens of times yielded the inter-raft potential (Methods). The effective repulsive potential is described by an exponential with a characteristic length scale of 0.65 μm (Fig. 3a). The measured raft–raft interactions can be quantitatively related to raft-induced membrane distortions visualized with a quantitative polarized light microscope (LC-PolScope). This technique yields images whose intensity indicates the local retardance, which is related to the local tilt of rods away from the membrane normal vector (Fig. 3c)[23]. The interior of a homogeneous one-component membrane viewed in the x–y plane lacks optical anisotropy and appears dark in the LC-PolScope. In contrast, rafts imaged with the LC-PolScope had a spatially varying retardance, indicating local twisting of raft-bound rods.

Such deformations can be understood by considering that *fd*-Y21M and M13KO7 have right-handed and left-handed chirality, respectively[19,24]. As a consequence, the interaction energy between membrane-embedded viruses is minimized when neighbouring rods are not parallel to each other but are twisted at a small but finite angle. The radially averaged retardance profile reveals that, starting from the raft centre, *fd*-Y21M rods twist with a right-handed sense, leading to increasing rod tilt away from the monolayer normal. The tilt attains a maximum at the raft's edge. Moving past the edge, the membrane is enriched in left-handed M13KO7. The left-handed twist induces tilting of rods back towards the membrane normal. Larger rafts attain a larger maximum edge tilt; however, the characteristic length over which twist penetrates into the background membrane is independent of raft size (Fig. 3d, e). The length scales associated with raft repulsion and raft-induced twist deformation are comparable, suggesting a possible link.

Homo-chiral colloidal membranes are inherently frustrated, because the constituent rods cannot simultaneously twist locally and assemble into a monolayer globally. Consequently, twist is expelled from the membrane interior to the edges. Increasing the rod chirality raises the free energy of interior untwisted rods while lowering the free energy of edge-bound twisted rods, leading to chiral control of edge line tension[25,26]. For uniformly mixed binary membranes, the same constraints enforce untwisting of all constituent chiral rods, thus raising their free energy. However, the formation of right-handed rafts in the left-handed background allows twist to penetrate into the membrane interior, lowering raft free energy. Besides explaining raft stability, this picture also explains the origin of inter-raft repulsion. Bringing two rafts together closer than the twist penetration length requires energetically costly untwisting of chiral rods. Our hypothesis predicts that the range of raft repulsion is independent of cluster size, while its strength increases linearly with cluster size. Measured potentials between clusters of different sizes agree with these predictions (Fig. 3a, b). Furthermore, when the magnitude of the repulsive interactions is rescaled by the maximum twist at the rafts edge obtained from LC-PolScope images, all potentials collapse on top of each other, thus establishing a quantitative relationship between raft-induced chiral distortions and membrane-mediated raft interactions. These experiments describe how chirality stabilizes finite-sized rafts, a mechanism that is complementary to other proposed mechanisms[27–29].

The emergent raft repulsions can be used to assemble higher-order structures. To explore this capability, we measured the raft radial distribution function, $g(r)$, for samples with increasing raft density (Supplementary Video 6). In the dilute limit, $g(r)$ is zero for small separations, indicative of strong repulsive interactions, and constant elsewhere (Fig. 4a). At intermediate raft densities, $g(r)$ exhibits liquid-like oscillations that decay after a few coordination shells (Fig. 4b). At highest densities, rafts form two-dimensional crystal-like structures as demonstrated by sharp peaks in $g(r)$ (Fig. 4c). This behaviour is reminiscent of conventional two-dimensional repulsive colloids. However, there are also important differences, because colloidal crystals are assembled from immutable solid particles whereas the membrane-embedded crystals are assembled from highly adaptable, size-adjustable rafts, each of which constantly exchanges rods with the background. Moreover, whereas conventional droplets in bulk suspensions always assume a surface-minimizing spherical shape, the behaviour of rafts embedded in a membrane is significantly more complex. For example, at higher ionic strength (125 mM) and depletant concentration (40 mg ml^{-1} and above), the interactions between rafts are no longer purely repulsive. Instead, as two rafts approach each other they can form a stable bond that takes a shape of a thin liquid bridge. Such processes lead to the formation of raft dimers, trimers and higher-order structures, which remain stable for many days (Fig. 4d and Supplementary Video 7). It is even possible to observe the assembly of highly complex structures such as a classical bead-spring polymer formed from nine raft subunits. The resulting polymer-like structure exhibits large fluctuations in shape; a quantitative analysis of these fluctuations reveals that the preferred angle of the neighbouring bonds is 109° (Fig. 4e and Supplementary Video 8).

Thus, we have demonstrated that chirality is important in the formation of thermodynamically stable, finite-sized, monodisperse rafts and their assembly into higher-order structures through membrane-mediated repulsive interactions that are orders of magnitude longer in range than attractive depletion interactions[30]. The chiral molecule cholesterol is known to be essential for the assembly of lipid rafts in biological membranes. However, our membranes comprised two oppositely twisted chiral colloids, whereas biological membranes contain only one

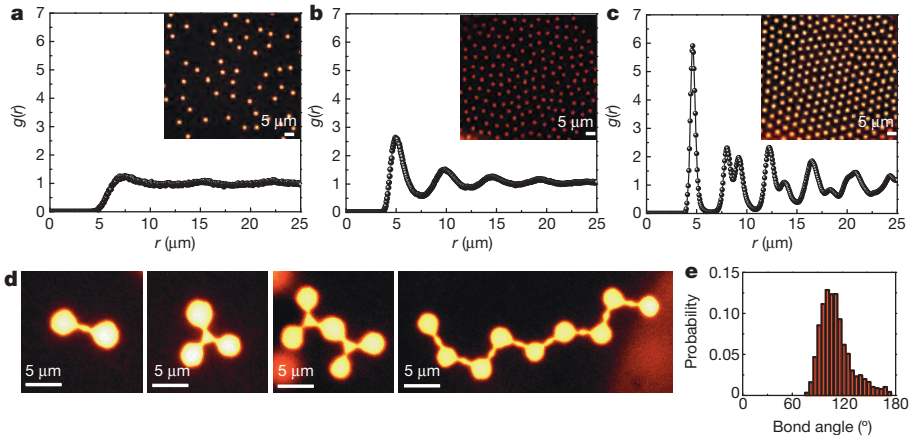

Figure 4 | Assembly of raft crystals and aspherical supra-rafts. **a**, Radial distribution function, $g(r)$, of dilute membrane-embedded clusters. The stoichiometric ratio of M13KO7 to *fd*-Y21M is 6:1. Inset: representative image of the membrane. **b**, At intermediate raft densities $g(r)$ exhibits a liquid-like structure (ratio of M13KO7 to *fd*-Y21M 4:1). **c**, At high densities, rafts organize into a two-dimensional cluster crystal (ratio of M13KO7 to *fd*-Y21M 2.2:1). **d**, Rafts can be permanently bonded by thin liquid bridges to form complex architectures. Fluorescence images of a raft dimer, trimer, pentamer and polymer-like nonamer are shown. **e**, Probability distribution of bond angles in the bead-spring nonamer obtained by analysing 400 independent configurations of the fluctuating polymer.

chiral constituent; the possible biological relevance of the chiral effects we have documented therefore remains an open question.

Online Content Methods, along with any additional Extended Data display items and Source Data, are available in the online version of the paper; references unique to these sections appear only in the online paper.

Received 14 May; accepted 14 July 2014.

1. ten Wolde, P. R. & Frenkel, D. Enhancement of protein crystal nucleation by critical density fluctuations. *Science* **277,** 1975–1978 (1997).
2. Hyman, A. A. & Simons, K. Beyond oil and water-phase transitions in cells. *Science* **337,** 1047–1049 (2012).
3. Stradner, A. *et al.* Equilibrium cluster formation in concentrated protein solutions and colloids. *Nature* **432,** 492–495 (2004).
4. Groenewold, J. & Kegel, W. K. Anomalously large equilibrium clusters of colloids. *J. Phys. Chem. B* **105,** 11702–11709 (2001).
5. Goulian, M., Bruinsma, R. & Pincus, P. Long-range forces in heterogeneous fluid membranes. *Europhys. Lett.* **23,** 155 (1993).
6. Dan, N., Berman, A., Pincus, P. & Safran, S. A. Membrane-induced interactions between inclusions. *J. Phys. II* **4,** 1713–1725 (1994).
7. Weis, R. M. & McConnell, H. M. Two-dimensional chiral crystals of phospholipid. *Nature* **310,** 47–49 (1984).
8. Dietrich, C. *et al.* Lipid rafts reconstituted in model membranes. *Biophys. J.* **80,** 1417–1428 (2001).
9. Dinsmore, A. D. *et al.* Colloidosomes: selectively permeable capsules composed of colloidal particles. *Science* **298,** 1006–1009 (2002).
10. Lin, Y., Skaff, H., Emrick, T., Dinsmore, A. D. & Russell, T. P. Nanoparticle assembly and transport at liquid–liquid interfaces. *Science* **299,** 226–229 (2003).
11. Veatch, S. L. & Keller, S. L. Separation of liquid phases in giant vesicles of ternary mixtures of phospholipids and cholesterol. *Biophys. J.* **85,** 3074–3083 (2003).
12. Baumgart, T., Hess, S. T. & Webb, W. W. Imaging coexisting fluid domains in biomembrane models coupling curvature and line tension. *Nature* **425,** 821–824 (2003).
13. Lingwood, D. & Simons, K. Lipid rafts as a membrane-organizing principle. *Science* **327,** 46–50 (2010).
14. Meng, G. N., Arkus, N., Brenner, M. P. & Manoharan, V. N. The free-energy landscape of clusters of attractive hard spheres. *Science* **327,** 560–563 (2010).
15. Chen, Q. *et al.* Supracolloidal reaction kinetics of Janus spheres. *Science* **331,** 199–202 (2011).
16. Wang, Y. F. *et al.* Colloids with valence and specific directional bonding. *Nature* **491,** 51–55 (2012).
17. Sarasij, R. C., Mayor, S. & Rao, M. Chirality-induced budding: a raft-mediated mechanism for endocytosis and morphology of caveolae? *Biophys. J.* **92,** 3140–3158 (2007).
18. Barry, E. & Dogic, Z. Entropy driven self-assembly of nonamphiphilic colloidal membranes. *Proc. Natl Acad. Sci. USA* **107,** 10348–10353 (2010).
19. Barry, E., Beller, D. & Dogic, Z. A model liquid crystalline system based on rodlike viruses with variable chirality and persistence length. *Soft Matter* **5,** 2563–2570 (2009).
20. Sprague, B. L., Pego, R. L., Stavreva, D. A. & McNally, J. G. Analysis of binding reactions by fluorescence recovery after photobleaching. *Biophys. J.* **86,** 3473–3495 (2004).
21. Gasser, U., Weeks, E. R., Schofield, A., Pusey, P. N. & Weitz, D. A. Real-space imaging of nucleation and growth in colloidal crystallization. *Science* **292,** 258–262 (2001).
22. Crocker, J. C. & Grier, D. G. Microscopic measurement of the pair interaction potential of charge-stabilized colloid. *Phys. Rev. Lett.* **73,** 352–355 (1994).
23. Barry, E., Dogic, Z., Meyer, R. B., Pelcovits, R. A. & Oldenbourg, R. Direct measurement of the twist penetration length in a single smectic A layer of colloidal virus particles. *J. Phys. Chem. B* **113,** 3910–3913 (2009).
24. Tombolato, F., Ferrarini, A. & Grelet, E. Chiral nematic phase of suspensions of rodlike viruses: left-handed phase helicity from a right-handed molecular helix. *Phys. Rev. Lett.* **96,** 10.1103/PhysRevLett.96.258302 (2006).
25. Gibaud, T. *et al.* Reconfigurable self-assembly through chiral control of interfacial tension. *Nature* **481,** 348–351 (2012).
26. Kaplan, C. N. & Meyer, R. B. Colloidal membranes of hard rods: unified theory of free edge structure and twist walls. *Soft Matter* **10,** 4700–4710 (2014).
27. Rozovsky, S., Kaizuka, Y. & Groves, J. T. Formation and spatio-temporal evolution of periodic structures in lipid bilayers. *J. Am. Chem. Soc.* **127,** 36–37 (2005).
28. Reynwar, B. J. *et al.* Aggregation and vesiculation of membrane proteins by curvature-mediated interactions. *Nature* **447,** 461–464 (2007).
29. Ursell, T. S., Klug, W. S. & Phillips, R. Morphology and interaction between lipid domains. *Proc. Natl Acad. Sci. USA* **106,** 13301–13306 (2009).
30. Seul, M. & Andelman, D. Domain shapes and patterns—the phenomenology of modulated phases. *Science* **267,** 476–483 (1995).

Supplementary Information is available in the online version of the paper.

Acknowledgements We acknowledge discussions with R. B. Meyer. This work was supported by the US National Science Foundation (NSF-MRSEC-0820492, NSF-DMR-0955776 and NSF-MRI-0923057) and the Petroleum Research Fund (ACS-PRF 50558-DNI7). We acknowledge use of the Brandeis MRSEC optical microscopy facility.

Author Contributions P.S., A.W. and Z.D. conceived and designed the experiments. P.S. and A.W. performed the experiments. M.F.H. designed the theoretical models. P.S., A.W., Z.D. and M.F.H. interpreted the experiments. T.G. provided material samples. P.S. and Z.D. wrote the manuscript.

Author Information Reprints and permissions information is available at www.nature.com/reprints. The authors declare no competing financial interests. Readers are welcome to comment on the online version of the paper. Correspondence and requests for materials should be addressed to Z.D. (zdogic@brandeis.edu).

METHODS

Virus growth and sample preparation. For our experiments we prepared a number of different viruses of varying contour length, chirality and persistence length including: *fd-wt* (wild type), *fd*-Y21M, M13KO7, M13-wt (wild type), M13mp18, *fd-tet* and Litmus phagemid grown with M13KO7 helper phage[19]. In preliminary investigations we explored six different mixtures: *fd*-Y21M and M13KO7, M13-wt and M13KO7, M13mp18 and M13KO7, *fd-wt* and *fd-tet*, *fd-wt* and M13KO7, and *fd-wt* and Litmus phagemid. In all these mixtures we found that stable microphase separation was located between uniformly mixed membranes at low depletant concentrations and bulk separation at high concentration. To make progress we primarily focused on a mixture of filamentous bacteriophages *fd*-Y21M and M13KO7. The rod-like *fd*-Y21M virus has a diameter of 6 nm, a contour length of 880 nm and a persistence length of 9.9 μm (ref. 19). M13KO7 has the same diameter but a contour length of 1,200 nm and a persistence length of 2.8 μm (ref. 31). Both systems exhibit isotropic, cholesteric and smectic phases with increasing virus concentration. However, *fd*-Y21M forms a cholesteric phase with a right-handed twist, whereas the M13KO7 cholesteric phase twists in the opposite direction[19,24].

M13KO7 and *fd*-Y21M viruses were purified using standard biological protocols[32]. To remove end-to-end dimers or longer viruses that destabilize colloidal membranes, purified virus suspensions were fractionated trough the isotropic–nematic phase transition[20]. Only the isotropic fraction, enriched in nominal length viruses, was used for assembling colloidal membranes. Viruses were suspended in Tris-HCl buffer (20 mM pH 8.0) to which 100 mM NaCl was added to screen electrostatic interactions. For fluorescence visualization, primary amines of the major coat protein of *fd*-Y21M were labelled with amine reactive fluorophore (DyLight-NHS ester 550; Thermo Fisher)[33]. There are about 2,700 labelling sites available on the virus surface. However, each virus was labelled at a low volume fraction (~30 dye molecules per virus), ensuring that the labelling did not affect the system phase behaviour. *fd*-Y21M and M13KO7 were mixed at known stoichiometric ratios. The non-adsorbing polymer dextran (molecular mass 500,000 Da; Sigma-Aldrich) was added to this suspension, and the resultant suspension was injected into an observation chamber. The chamber was made from a microscope slide and a coverslip (Goldseal; Fisher Scientific) separated by a spacer consisting of a non-stretched Parafilm and sealed with ultraviolet-cured glue (Norland Optical). Glass surfaces were thoroughly cleaned with a hot 1% soap solution (Hellmanex; Hellma Analytics). Samples prepared in this manner remained stable for weeks or even months. The final concentration of bi-disperse virus mixture was 2.5 mg ml^{-1}. All the measurements were performed for membranes assembled at 40 mg ml^{-1} dextran concentration. Membranes initially assembled in the bulk suspension but owing to their density they eventually sedimented onto the coverslip. To prevent non-specific absorption, glass surfaces were coated with a polyacrylamide brush, which suppressed the depletion interaction between viruses and the glass walls[34].

Optical microscopy methods. Within a liquid-like colloidal monolayer membrane, rods with opposite chirality phases separated to form finite-sized colloidal rafts, with the exact behaviour depending on the depletant concentration. Raft structures and dynamics were examined with several complementary optical microscopy techniques. Differential interference contrast, phase contrast and fluorescence images were acquired using an inverted microscope (Nikon TE2000) equipped with an oil-immersion objective (1.3 numerical aperture, ×100 Plan-Fluor) and connected to charge-coupled-device camera (Andor Clara). Fluorescently labelled *fd*-Y21M virus was imaged using the same setup equipped with mercury–halide epifluorescence source and a rhodamine filter cube (excitation wavelength 532–554 nm, emission wavelength 570–613 nm). The exposure time for acquisition of fluorescent images was 100 ms.

Spatial variations of rod tilt with respect to the membrane normal were determined using an LC-Polscope (Cambridge Research and Instrumentation)[35]. The LC-PolScope yields images in which the intensity of each pixel is proportional to local sample birefringence. Subtraction of the background birefringence enabled the visualization of subnanometre birefringent images with LC-PolScope, something that is not possible with conventional techniques. For a membrane lying in the image plane, it is possible to translate the LC-PolScope birefringence signal quantitatively into local tilting of the rods away from the membrane normal[23,36].

Determination of k_{off} using single-raft FRAP. DyLight 550 attached to *fd*-Y21M surface has an excitation wavelength of 562 nm. An isolated raft of predetermined size enriched with fluorescently labelled *fd*-Y21M was illuminated with a focused laser beam (~100 mW, 514 nm). Under these conditions, raft-bound rods bleached instantaneously for all practical purposes. The exchange of rods between rafts and the background membrane caused fluorescence to recover on a timescale of minutes. This process can be modelled using kinetic equations. $N_f(t)$ and $N_b(t)$, respectively, describe the number of fluorescent and bleached rods in a raft at time t. Assuming that the raft size does not change on fluorescence recovery timescales and that the concentration of bleached rods in the membrane background is negligible, the time evolution of $N_f(t)$ and $N_b(t)$ is given by

$$\frac{dN_f(t)}{dt} = -k_{off}N_f(t) + k_{on}C_{BG}$$

$$\frac{dN_b(t)}{dt} = -k_{off}N_b(t)$$

where k_{off} and k_{on} are rod dissociation and association rates and C_{BG} is the concentration of fluorescent *fd*-Y21M rods in the background membrane[20]. The experimentally measured total raft intensity is given by $I_{tot}(t) = \alpha N_f(t) + \beta N_b(t)$, where α and β are the intensities of single fluorescently labelled and bleached viruses, respectively. Perfect bleaching would result in $\beta = 0$. However, we found that this not the case: bleached rods retained finite fluorescence. Solving for $I_{tot}(t)$ yields

$$I_{tot}(t) = \exp(-k_{off}t)\left(I_0 - I_{av}^{BG}k_{on}/k_{off}\right) + I_{av}^{BG}k_{on}/k_{off} \quad (1)$$

where I_0 is the raft fluorescence intensity after completion of the photo-bleaching event and I_{av}^{BG} is the mean fluorescence intensity of the background membrane. Equation (1) shows that the fluorescence recovery process can be approximated by a single-exponential rate, in agreement with experimental findings. The exponential time constant yields the rod dissociation constant $1/k_{off}$ (Fig. 2e, h).

Evolution of polydisperse rafts yields k_{on}. Heterogeneously sized rafts evolved towards equilibrium, a state characterized by rafts of uniform size. Using optical tweezers we fragmented/fused a small fraction of rafts, thus creating an artificially polydisperse population, and then quantified their subsequent size evolution. The long-time-lapse videos required for this measurement were acquired on a microscope equipped with auto-focus capabilities (Perfect-Focus; Nikon Ti-E). The rate equation governing the evolution of raft size is

$$\frac{dN(t)}{dt} = -k_{off}N(t) + k_{on}C_{BG} \quad (2)$$

where $N(t)$ is the total number of raft bound rods at time t. Cluster size evolution experiments yielded $dN(t)/dt$ and $N(t)$ (Fig. 2g), C_{BG} was extracted from fluorescent membrane images, and k_{off} and its size were obtained from previously described single-raft FRAP measurements. It follows that k_{on} and its dependence on raft size can be uniquely determined from equation (2), because all other parameters are determined from independent experiments.

Measuring the raft free-energy landscape. The change in free energy, ΔG, required to add a single rod to a raft containing N rods is given by

$$k_{on}/k_{off} = A_{rod}Ne^{-\Delta G/k_BT} \quad (3)$$

where A_{rod} is the effective area occupied by a single *fd*-Y21M virus, N is the number of rods in a raft and $A_{rod}N$ is the raft size. Assuming dilute suspension conditions, the chemical potential of *fd*-Y21M rods dissolved in the background membrane is given by $\mu = k_BT\ln(C_{BG}A_{rod})$. The net change in free energy associated with taking a single *fd*-Y21M virus from the background and inserting it into a raft containing N rods is given by $\Delta G - \mu$ (Fig. 2i, inset). The absolute raft free-energy landscape up to a constant offset was obtained by numerically integrating $\Delta G - \mu$ with the use of a cumulative trapezoidal rule (Fig. 2i).

Single-molecule analysis. We prepared raft-bearing membranes with non-fluorescent long and short rods. These membranes were doped with a very low volume fraction of fluorescent short rods (~0.003%) enabling us to visualize the motion of single rods within the membrane background and rafts. The membranes were simultaneously visualized in phase contrast and fluorescence microscopy to determine the number of raft-bound labelled rods, N_f. Standard analysis shows that the decay of the autocorrelation function of N_f is given by $\langle N_f(t)N_f(t+\Delta t)\rangle - \langle N_f(t)\rangle^2 = (k_{on}C_{BG}/k_{off})e^{-k_{off}t}$ (ref. 37). Therefore k_{off} and k_{on} can be determined uniquely with this expression. These measurements were performed for equilibrium-sized rafts only.

Measurement of membrane-mediated repulsive raft interactions. To measure effective raft–raft interactions, we used the blinking optical trap technique originally developed for measuring effective potentials of conventional spherical colloids[24]. Being enriched in shorter *fd*-Y21M rods, rafts are repelled from an optical trap. To manipulate these rafts, we created an optical plough-like configuration consisting of multiple time-shared optical traps generated by an acousto-optic deflector. Using a pair of optical ploughs we brought two rafts into close proximity (Supplementary Video 5). Once the traps were switched off, the repulsive membrane-mediated interactions drove the rafts apart. It was possible to measure these interactions by repeating the blinking experiment dozens of times and analysing the time evolution of subsequent raft trajectories. Focusing an optical trap onto a membrane induces local distortions that could potentially affect the measurement of raft interactions. This made it advantageous to measure interactions using blinking optical traps. In this technique, the traps are only used to bring two rafts into an initial low-probability configuration, but the actual measurement is performed when the optical traps are switched off. On switching the laser off, the trap-induced membrane distortions

relaxed on a millisecond timescale, which is essentially instantaneous when compared with the timescale of minutes over which two repulsive rafts drift apart.

Optical plough trap configurations were generated by time sharing a laser beam (4W, 1064 nm, Compass 1064, Coherent) using a pair of orthogonally oriented paratellurite acousto-optic deflectors (Intra-Action). The laser beam was projected onto the back focal plane of an oil-immersion objective (1.3 numerical aperture, ×100 PlanFluor) and focused onto the imaging plane. The multiple trap locations were specified with a custom LABVIEW software. Raft separations were measured as a function of time, once the traps had been switched off, using standard video tracking methods[38]. The time lapse between successive frames was 100 ms and the exposure time was 50 ms.

The discretized probability of a raft pair's being separated by distance r_j at time $t + \Delta t$ is given by

$$\rho(r_j) = \sum_i P(r_i \rightarrow r_j)\rho(r_i)$$

where P is the transition probability for a raft pair initially separated by distance r_i at time t to be separated by distance r_j at time $t + \Delta t$ later. $\rho(r_i)$ is the probability of a raft pair's being separated by a distance r_i at time t (ref. 22). Experimentally, P is determined by binning the trajectories according to the initial and final separations in each time step. The steady-state solution to equation (1) is equal to the equilibrium probability, $\rho(r)$, computed by calculating the eigenvector of the transition probability matrix. The inter-raft potential is given by $U(r) = -k_B T \ln(\rho(r))$.

31. Dogic, Z. & Fraden, S. Development of model colloidal liquid crystals and the kinetics of the isotropic–smectic transition. *Phil. Trans. R. Soc. A* **359,** 997–1014 (2001).
32. Maniatis, T., Sambrook, J. & Fritsch, E. *Molecular Cloning* (Cold Spring Harbor Laboratory, 1989).
33. Lettinga, M. P., Barry, E. & Dogic, Z. Self-diffusion of rod-like viruses in the nematic phase. *Europhys. Lett.* **71,** 692–698 (2005).
34. Lau, A. W. C., Prasad, A. & Dogic, Z. Condensation of isolated semi-flexible filaments driven by depletion interactions. *Europhys. Lett.* **87,** 48006 (2009).
35. Oldenbourg, R. & Mei, G. New polarized-light microscope with precision universal compensator. *J Microsc.* **180,** 140–147 (1995).
36. Zakhary, M. J. *et al.* Imprintable membranes from incomplete chiral coalescence. *Nature Commun.* **5,** http://dx.doi.org/10.1038/ncomms4063 (2014).
37. Gardiner, C. W. *Handbook of Stochastic Methods* (Springer, 1985).
38. Crocker, J. C. & Grier, D. G. Methods of digital video microscopy for colloidal studies. *J. Colloid Interf. Sci.* **179,** 298–310 (1996).